Low-Cost Methodology for Series Resistance Spatial Characterization in PV Devices Through Electroluminescence Imaging

José Raymundo de Alcântara Neto[1], Adriano Moraes da Silva[1] and Douglas Bressan Riffel[1]

[1] Federal University of Sergipe, São Cristóvão (Brazil)

Abstract

This work proposes an integrated, low-cost methodology for the spatial characterization of series resistance (R_s) in photovoltaic (PV) devices through electroluminescence (EL) imaging using commercial digital cameras. The approach includes the development of a procedure for selecting optimal ISO and exposure time settings according to image quality requirements defined by international standards, as well as a systematic method for accurate focus determination during EL image acquisition. Established image preprocessing and calibration techniques were integrated with existing R_s estimation models, enabling both global and spatially resolved resistance mapping, where each pixel represents a local R_s value. The proposed methodology enhances the accessibility and accuracy of EL-based diagnostics, supporting performance analysis, degradation assessment, and fault detection in PV systems. Additionally, the method provides a reproducible workflow in accordance with international standards suitable for laboratory and field applications.

Keywords: Low-cost electroluminescence imaging; Electroluminescence image calibration; Series resistance in photovoltaic devices; Spatially resolved series resistance; Photovoltaic diagnostics

1. Introduction

Series resistance (Rs) in photovoltaic (PV) devices is a key parameter influencing energy conversion efficiency. Elevated Rs values lead to power losses, especially under high irradiance conditions, and may indicate degradation or manufacturing defects. Electroluminescence (EL) imaging has proven to be a powerful, non-destructive technique for detecting such resistive losses (Potthoff et al., 2010). However, the high cost of scientific-grade equipment limits its widespread use in field diagnostics and routine quality assessments.

To overcome this limitation, several studies have explored alternative imaging systems employing low-cost commercial digital cameras based on Charge-Coupled Devices (CCD), as demonstrated by Figueiredo and Pinho Almeida (2018). Furthermore, Potthoff et al. (2010) and Kropp et al. (2018) proposed methodologies for analyzing PV modules through EL imaging, enabling the extraction of critical parameters such as series resistance (Rs) and the identification of defects and degradation patterns.

Building upon these contributions, the present study aims to democratize access to EL-based diagnostics by proposing a methodology that combines low-cost imaging hardware with tailored acquisition and processing techniques. Specifically, the work addresses three main challenges: (1) determining optimal camera settings for image quality compliance; (2) defining a repeatable method for EL image focusing; and (3) integrating image preprocessing and calibration methods with Rs estimation algorithms to generate spatial resistance maps.

2. Methodology

2.1 Electroluminescence Image Acquisition

Electroluminescence (EL) images were acquired under control conditions in a custom dark chamber. The photovoltaic device, a Komaes Solar KM(P)5 5W polycrystalline PV module, was positioned at 33 cm from the camera lens and aligned normally to the optical axis. The setup employed a Canon EOS Rebel SL3 (D250)

10.18086/swc.2025.03.41 Available at http://proceedings.ises.org

camera equipped with a 35 mm focal length lens, mounted on a fixed support and remotely operated via Canon EOS Utility® software.

During image acquisition, the PV module was forward-biased using a programmable DC power supply (Agilent E3631A) adjusted to the desired short-circuit current (I_{sc}) level. After setting the current level, the forward bias was applied, and a 60-second stabilization period was allowed for the electroluminescent emission to reach a steady state. Once this stabilization time elapsed, the camera shutter was triggered for the selected ISO and exposure time, capturing two sequential dark EL images at each I_{sc} level for subsequent processing.

Two I_{sc} levels — 10% and 100% — were applied in accordance with the reference methodology adopted in this work. Additionally, a background image was acquired under identical dark EL camera settings to support image quality evaluation.

2.2 Optimization of Image Acquisition Parameters

To optimize image quality, ISO and exposure time combinations were evaluated with reference to the IEC TS 60904-13 standard (IEC, 2019), which establishes minimum image quality requirements for electroluminescence (EL) measurements based on the signal-to-noise ratio (SNR_{50}).

In addition to the standard metric, a complementary analysis of relative pixel saturation was introduced to identify acquisition settings that maintained sufficient brightness without overexposing pixel regions, ensuring data reliability for subsequent processing.

Initial ISO and exposure time values were defined according to the camera sensitivity limitations, and additional combinations were tested to maintain consistent average pixel intensity. The best configuration was determined by maximizing SNR_{50} while minimizing relative pixel saturation.

2.2 Focus-assistance Procedure

Due to the low-light conditions in Dark EL imaging and longer time necessary for the capture of an image in a low-cost commercial camera, manual focusing on a trial-and-error approach can be very time-consuming or even unreliable. A novel method based on preliminary visible light and dark EL captures associations and sharpness quantification was implemented.

The focal relationship between the cited two types of images was determined. To do that several visible light images with different focus were captured and their sharpness was determined by the Tenengrad gradient. Just after each visible light image, one Dark EL image was captured at the same focus and its sharpness was also determined. With that the direct association between the two sharpness at the same focus allowed one to find the sharpest Dark EL image by manually varying focus at visible light image captures and finding the image with approximated sharpness to that with the sharpness at the same focus as the better Dark EL empirically found.

2.3 Image Pre-Processing and Calibration

After the image acquisition process, the captured dark electroluminescence (EL) images were subjected to a preprocessing stage aimed at improving their quality and ensuring consistency across measurements (Figure 1). These steps included single-time effect correction, background subtraction, flat-field correction, and artefact removal, following the methodology described by Bedrich (2017).

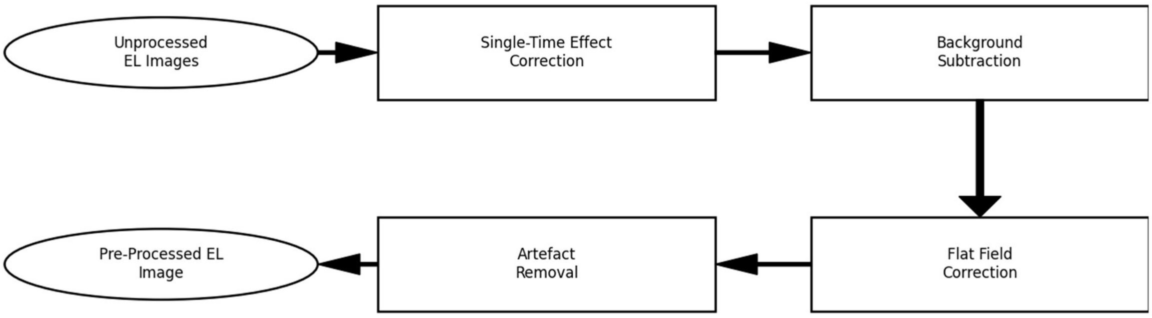

Figure 1. Flowchart of the dark electroluminescence (EL) image preprocessing steps. The diagram summarizes the sequence of correction and filtering operations applied to improve image uniformity and ensure compliance with IEC TS 60904-13 (2019), including single-time-effect correction, background subtraction, flat-field correction, and artifact removal.

2.4 Image Segmentation

To estimate the series resistance within the regions corresponding to the photovoltaic cells, image segmentation was employed. The segmentation process was performed manually on images captured under visible light, ensuring accurate delineation of each cell boundary and minimizing potential errors in subsequent processing steps.

The individual cell contours were manually annotated using a Python-based tool, resulting in a set of binary masks — one for each identified cell. Since the primary objective of this work was not to develop or optimize segmentation algorithms, a simplified methodological approach was adopted. The process was limited to the generation of these segmentation masks, which were then directly applied to the electroluminescence (EL) images captured under the same geometric configuration.

This procedure enabled a precise spatial correspondence between the visible-light and EL datasets and ensured that each cell region could be independently analyzed in the following resistance estimation and mapping steps

2.5 Series Resistance Estimation and Mapping

Module's total series resistance ($R_{s,\,mod}$) was estimated from the processed electroluminescence (EL) images following the image-based procedure described by Potthoff et al. (2010). In that method, Rs,mod is inferred by relating local variations in EL intensity to the voltage drop across the module through an exponential relation between intensity and junction voltage. In this work, the method was partially applied, implementing only the image-based $R_{s,\,mod}$ estimation stage. The calibration and measurement stages from the original procedure were not included. The approach was applied to residual EL images, combined with the preprocessing pipeline described previously to enhance contrast and ensure compatibility with low-intensity data.

The resulting $R_{s,\,mod}$ values were compared to those obtained through analytical estimations using datasheet parameters (Villalva et al., 2009) and from experimental IV curve slopes, both of which are well-established reference methods for $R_{s,\,mod}$ evaluation.

Subsequently, the spatial series resistance (R_s) map was generated following the procedure described by Kropp et al. (2018), which converts EL images into locally resolved series-resistance distributions. In the original method, the $R_{s,\,mod}$ is taken from the datasheet to scale the resistance map and simulate module performance. In this study, only the mapping stage of the method was applied, while $R_{s,\,mod}$ was replaced by values obtained from independent estimation approaches—namely, the analytical model of Villalva et al. (2009), the experimental I–V curve slope, and the image-based approach of Potthoff et al. (2010). This partial application enabled the construction and comparison of pixel-wise R_s distributions, providing a spatial analysis of resistive behavior under distinct estimation assumptions.

The complete workflow for the $R_{s,\,mod}$ estimation and R_s mapping process is summarized in Figure 2, which illustrates the integration of preprocessing, R_s estimation, and spatial mapping stages.

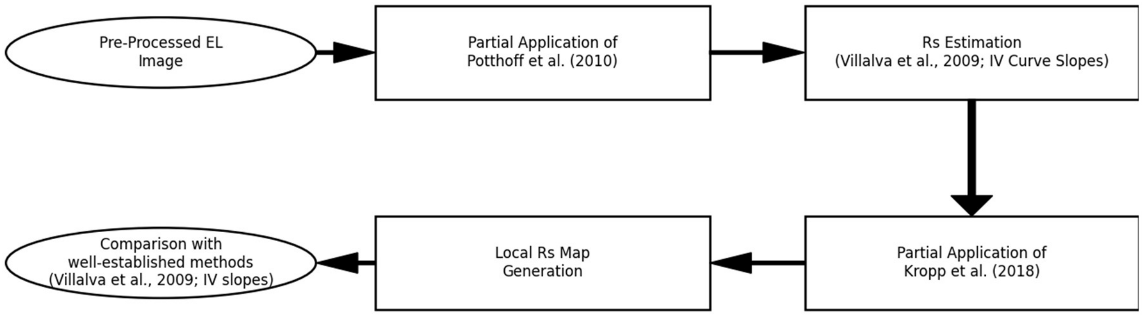

Figure 2. Flowchart of the series resistance (Rs) estimation and mapping procedures. This diagram illustrates the overall workflow for $R_{s,\,mod}$ estimation, showing the adapted methodology from Potthoff et al. (2010), the analytical comparison with Villalva et al. (2009) and I–V-curve slope methods, and the integration into the Kropp et al. (2018) framework for generating the spatial Rs map.

3. Results and Discussion

3.1 Optimization of Image Acquisition Parameters

Following the optimization procedure described in Section 2.2, several ISO and exposure-time combinations were tested to evaluate image quality performance under the IEC TS 60904-13 (2019) recommendations.

Table 1 lists the configurations that produced SNR_{50} values closest to the standard's minimum requirement (SNR_{50} > 45). The first configuration meets this criterion and shows the best per-channel pixel saturation behavior, although its average pixel intensity was low.

Table 1: ***Electroluminescence image acquisition parameters for different ISO and exposure time settings used in this study.*** **This table presents the evaluated combinations of ISO and exposure times for dark EL imaging. The selected configuration (ISO 200, 480 s) achieved the best compromise between average pixel intensity, saturation level, and SNR_{50} > 45, ensuring compliance with IEC TS 60904-13 (2019) standards.**

ISO	Exposure Time [seconds]	Averaged Pixel Intensity	Relative Saturated Intensity (%)	SNR_{50}
200	240	76.06	0.00233	46.65
200	480	120.61	6.457783	58.20
400	240	121.07	7.105300	43.59
800	120	117.94	4.906738	40.52

The remaining configurations presented more balanced average intensities, with saturation levels below 8 %. Among them, only one configuration—besides the first—achieved SNR_{50} > 45.

Therefore, the last configuration (ISO 200, 480 s) was adopted for further analysis, as it ensured a suitable compromise between average pixel intensity, saturation level, and compliance with IEC TS 60904-13 image-quality recommendations.

3.2 Focusing Method

The focus-assistance procedure (Section 2.3) was evaluated by computing the Tenengrad sharpness metric at matched focus positions for visible-light and dark EL images.

Table 2 reports on the values measured. The dark EL series exhibits a clear maximum at position 3, whereas the visible-light series peaks at position 1. Although the maxima do not coincide—likely due to wavelength-dependent contrast and sensor response—the visible captures still narrow the search to a small focus interval, after which a single short EL check is sufficient to set the final focus.

Table 2: Tenengrad gradient values for visible-light and dark electroluminescence (EL) images at different focus positions.

Focus position	Tenengrad (Visible)	Tenengrad (Dark EL)
1	5,121	922
2	1,365	1,246
3	557	1,935
4	461	928
5	1,078	825

This two-step process reduces setup time and ensures consistent sharpness across EL captures. Moreover, once the optimal visible focus is established for a given setup, subsequent experiments on the same module—or on modules of the same model under identical configuration—require only verification of the visible image focus, followed by a single EL capture to confirm alignment. This makes the method particularly suitable for repetitive testing and long-term monitoring applications.

3.3 Image Preprocessing Results

The preprocessing stage significantly improved the visual quality of the dark EL images. As shown in Figure 3, the unprocessed image (a) exhibits non-uniform illumination and sensor artefacts, while the processed image (b) presents enhanced contrast, reduced artefacts, and improved background uniformity. The corrections resulted in clearer definition of the metallization lines and defect areas, providing reliable input for the subsequent Rs estimation analyses.

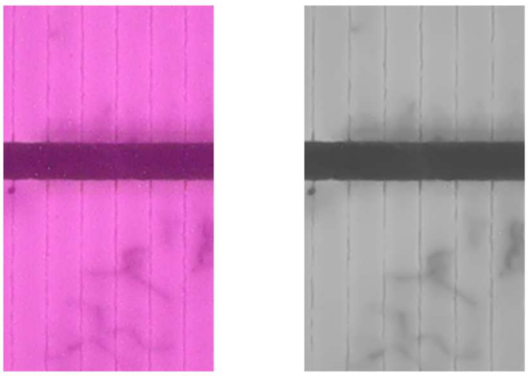

(a) (b)

Figure 3. Effect of preprocessing on a selected photovoltaic cell. Image (a) shows the original dark electroluminescence (EL) capture before corrections; image (b) presents the original dark electroluminescence (EL) capture converted to gray scale after applying single-time-effect removal, background subtraction, flat-field correction, and artefact removal. The result demonstrates improved uniformity and enhances overall contrast.

3.4 Segmentation Output

The segmentation process successfully isolated each photovoltaic cell region, enabling individual electrical analysis. As illustrated in Figure 4, the generated masks accurately matched the visible-light cell contours, ensuring full spatial correspondence between the EL and reference domains. This step provided the structural foundation for computing cell-by-cell R_s values and constructing spatial resistance maps.

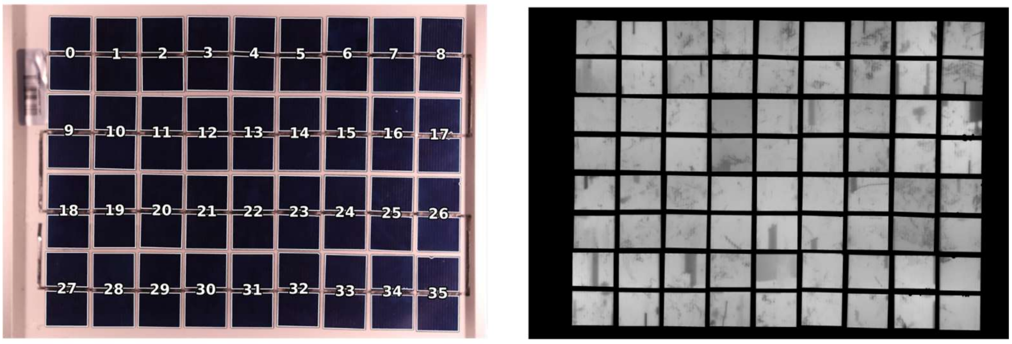

(a) (b)

Figure 4. Result of photovoltaic cell segmentation. Image (a) corresponds to the visible-light capture of the PV module with manually numbered cells; image (b) shows the segmented EL image using the generated masks, where each isolated cell region served as the basis for local series-resistance (Rs) estimation.

3.5 Series Resistance Estimation and Mapping

Once the segmentation stage was completed and each cell accurately isolated, the analysis proceeded with the estimation of module's total series resistance ($R_{s,\,mod}$) using both the electroluminescence-based approach adapted from Potthoff et al. (2010) and analytical models.

Using the dark electroluminescence (EL) image method, $R_{s,\,mod}$ was estimated at 5.20 Ω, while the analytical model proposed by Villalva et al. (2009) — based on datasheet parameters — yielded a slightly lower value of 5.08 Ω. The estimation derived from the slope of the experimental I–V curve resulted in a significantly higher $R_{s,\,mod}$ of 7.74 Ω.

A comparative summary of the results obtained from each estimation approach is presented in Table 2.

Table 2: Comparative summary of $R_{s,\,mod}$ estimation results obtained by different methods. The table summarizes the $R_{s,\,mod}$ values derived from three approaches: (i) the dark EL image method adapted from Potthoff et al. (2010), (ii) the analytical model of Villalva et al. (2009), and (iii) the I–V-curve slope. The comparison highlights the small deviation (≈ 3 %) between EL-based and datasheet-based results, and the larger difference (≈ 32 %) relative to the I–V slope estimate.

Estimation Method	Reference	Basis / Data Source	Estimated $R_{s,mod}$ [Ω]	Relative Difference [%]
Dark EL image method	Potthoff et al. (2010)	Residual EL image intensity distribution	5.20	—
Analytical model	Villalva et al. (2009)	Datasheet electrical parameters	5.08	-3
Experimental I–V slope	—	Linear regression of low-voltage region	7.74	+32

Compared to these reference methods, the $R_{s,\,mod}$ value obtained from dark EL imaging differed by approximately 3 % from the datasheet-based estimate and was about 32 % lower than that calculated from the

I–V curve. These differences highlight the distinct sensitivities of each approach to input data characteristics and measurement conditions.

The estimated EL-based $R_{s, mod}$ was subsequently integrated into the adapted Kropp et al. (2018) framework to generate the spatial resistance map, serving as the reference for local Rs calibration and defect correlation analysis.

To assess the consistency between the estimation approaches, the relative percentage series resistance maps generated using the module $R_{s, mod}$ values derived from the datasheet (5.076 Ω) and from electroluminescence (5.204 Ω) were compared. The two maps exhibited a high degree of agreement, with quantitative metrics of SSIM = 0.99998, MAE = 0.09299 Ω/cm², MSE = 0.01441 (Ω/cm²)², and r = 1, indicating nearly identical spatial patterns despite individual normalization.

The resulting R_s maps obtained from both estimation approaches are presented in Figure 5. Despite differences in the $R_{s, mod}$ inputs, both spatial distributions exhibit highly correlated patterns, confirming the consistency between methods.

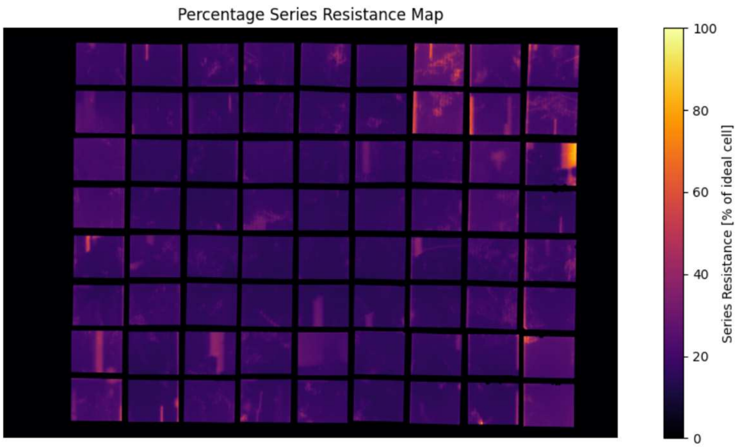

(a)

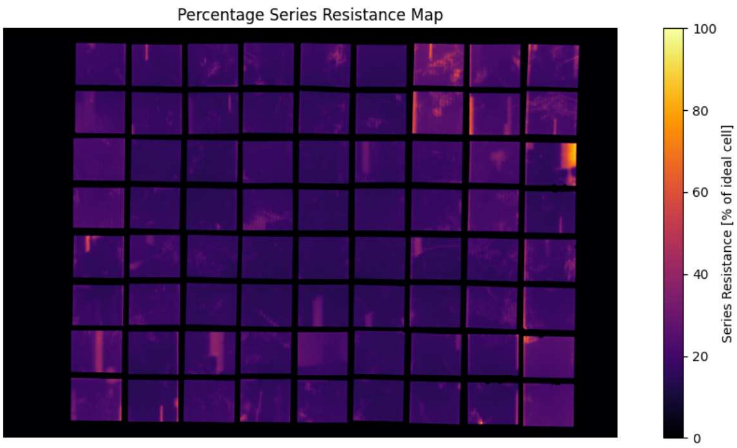

(b)

Figure 5: Spatial distribution of series resistance (R_s) obtained from the adapted Kropp et al. (2018) model. The maps generated using $R_{s, mod}$ values from the datasheet (5.076 Ω) (a) and from electroluminescence (5.204 Ω) (b) show nearly

identical spatial patterns, with SSIM = 0.99998, MAE = 0.09299 Ω/cm², and r = 1, confirming high consistency between estimation methods.

To provide a broader assessment, a comparative analysis was also performed including the $R_{s,\ mod}$ value obtained from the experimental I–V slope method. Table 3 summarizes the similarity metrics (SSIM, MAE, MSE, and Pearson's r) computed among all estimation methods, highlighting the spatial and statistical correspondence between the resulting relative percentage series resistance maps.

Table 3: Comparison metrics between relative percentage series resistance (R_s) maps obtained from different estimation methods. The table summarizes quantitative similarity measures between R_s maps derived from electroluminescence (EL), datasheet-based (Villalva et al., 2009), and I–V slope methods. High SSIM and r values indicate strong structural correlation, while higher MAE and MSE values for

Comparison	SSIM	MAE [Ω/cm²]	MSE [(Ω/cm²)²]	Relative Difference [%]
EL × Datasheet	0.99998	0.09299	0.01441	1.000
EL × I–V Slope	0.994	1.660	4.593	0.999
Datasheet × I–V Slope	0.994	1.567	4.093	0.999

In contrast, the map obtained using the $R_{s,\ mod}$ value estimated from the I–V slope at Voc (7.740 Ω) showed larger discrepancies relative to the others. Quantitatively, MAE ≈ 1.660 and 1.567 Ω/cm² and MSE ≈ 4.593 and 4.093 (Ω/cm²)² were observed, indicating greater pixel-by-pixel variability. Even so, SSIM ≈ 0.994 and r ≈ 0.999 still denote preservation of structural similarity across methods.

These results confirm that while absolute $R_{s,\ mod}$ values affect the resistance scale, the underlying spatial structures remain consistent. We conclude that normalization by the local maximum resistance enables structural comparison across methods, showing that all techniques capture similar spatial patterns of series resistance. Consequently, spatial information essentially depends on the EL image itself, which remains valuable for identifying loss-concentration regions and assessing coherence among methods.

The relative R_s map derived from the I–V-based estimation is shown in Figure 6, illustrating the higher overall scale but consistent spatial behavior.

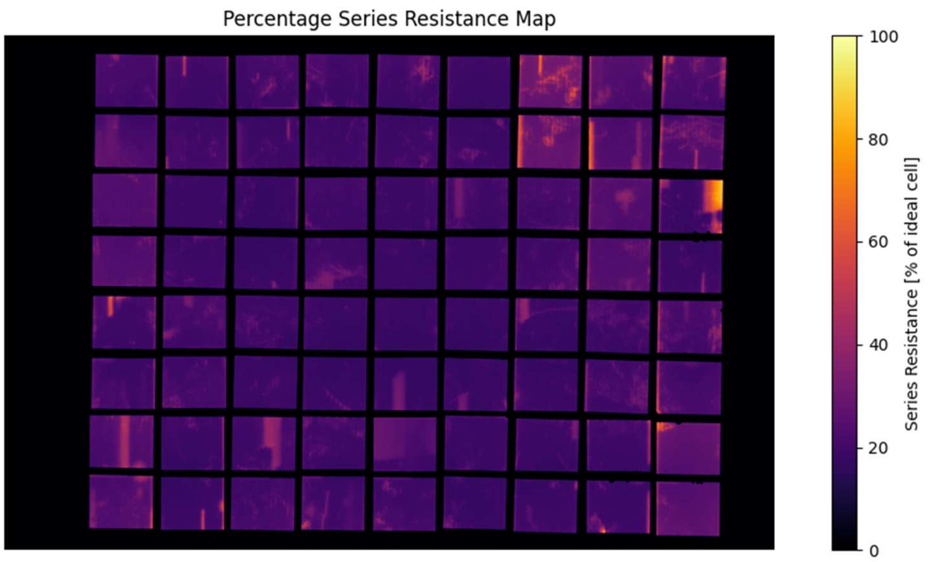

Figure 6. Relative percentage series resistance map derived from I–V-based Rs estimation ($R_{s,\ mod}$ = 7.740 Ω). Although the absolute resistance scale differs, the spatial distribution remains coherent with the previous maps, highlighting that EL-based information preserves structural correspondence across estimation approaches.

3.6 Equivalent Series Resistance per Cell

The equivalent series resistance per cell ($R_{s,\ cell}$) was reconstructed for each photovoltaic cell by summing the local resistance values obtained from the spatial absolute R_s maps, assuming series connectivity within and among cells. This reconstruction reflects the effective resistive behavior of the module under operational conditions.

Figure 7 presents the $R_{s,\ cell}$ derived from the EL-based $R_{s,\ mod}$ estimation ($R_{s,\ mod} = 5.204\ \Omega$). Peaks in the plot correspond to cells exhibiting higher resistive losses, while lower values indicate regions with more uniform conduction.

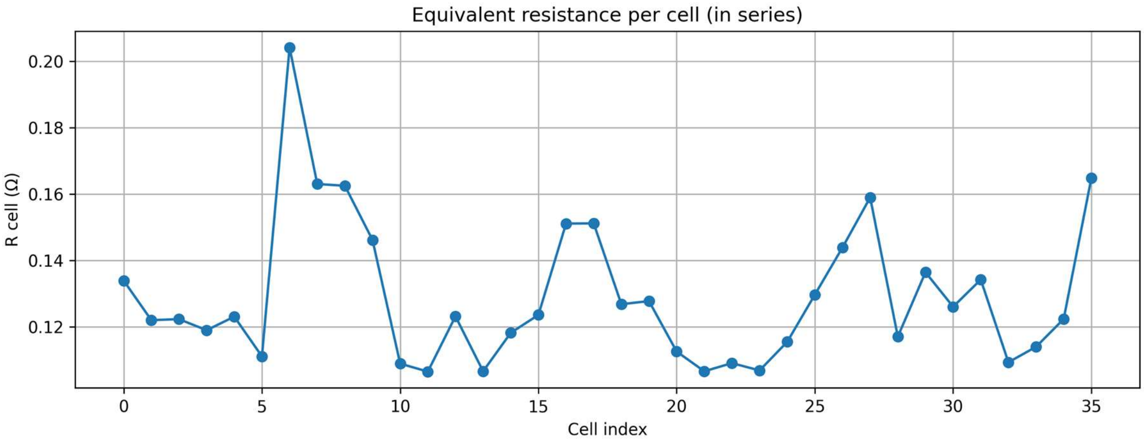

Figure 7. Equivalent series resistance per cell ($R_{s,\ cell}$) reconstructed from the spatial R_s map. Each point represents the cumulative series resistance of one photovoltaic cell. Higher peaks indicate regions with increased resistive losses, whereas lower values correspond to more uniform conduction across the module.

The adopted approach, combined with the series association between the cells, yielded values that were more consistent with those obtained through traditional Rs extraction techniques and showed greater adherence to the observed physical behavior (Fig. 7). The rationale for this modeling lies in the preferential current flow along each cell, driven by the alignment of the current toward the longitudinal metallic contacts (busbars and fingers).

Furthermore, in devices exhibiting non-uniform resistivity distributions—such as the photovoltaic device (PV) analyzed here, where variations in semiconductor material quality or localized degradation are present—the current tends to circumvent regions of higher resistivity, reinforcing the series nature of the overall electrical conduction.

It is important to emphasize that, although at a strictly local level it may be analytically convenient to represent conduction as occurring through multiple parallel paths, the series association of local resistances more accurately captures the cumulative ohmic losses observed experimentally. From a physical standpoint, there are no isolating barriers between neighboring regions that would prevent these voltage drops from summing along the current path, making the series representation the most appropriate for evaluating the $R_{s,\ cell}$.

4. Conclusion

This study presented a reproducible and low-cost methodology for the spatial characterization of series resistance (R_s) in photovoltaic (PV) modules using electroluminescence (EL) imaging. The proposed workflow combines optimized image acquisition parameters, a focus-assistance method based on visible-light imaging, and an image-processing pipeline for R_s estimation and mapping.

By analyzing ISO and exposure-time combinations according to the IEC TS 60904-13 standard, the methodology ensured compliance with the signal-to-noise ratio (SNR_{50}) requirements defined for EL imaging. Additionally, a complementary analysis of relative pixel saturation was introduced to identify the most suitable compromise between image brightness and data reliability.

The focus-assistance method proved effective in reducing acquisition time for subsequent measurements on the same module or modules of the same model and setup configuration, providing reproducible sharpness across captures. The spatial Rs mapping enabled the identification of locally distributed resistive regions within each cell, revealing variations among cells that reflect inherent manufacturing differences. Representing the results as a relative (percentage) resistance map increased the robustness of comparisons between estimation methods, since the absolute $R_{s,\ mod}$ values vary according to the chosen approach.

The technique therefore offers a practical framework for both laboratory and field applications, allowing spatial monitoring of resistive behavior over time. Repeated EL analyses using this method could support the early detection of degradation or defect evolution in PV modules.

5. Acknowledgments

The authors gratefully acknowledge the support from the LABENGE Research Group at the Federal University of Sergipe (UFS) and the Postgraduate Program in Electrical Engineering (PROEE/UFS). Financial assistance was provided by CAPES, FAPITEC, and a master's scholarship from National Council for Scientific and Technological Development (CNPq).

6. References

Bedrich, K.G., 2017. *Quantitative electroluminescence measurements of PV devices.* Doctoral thesis, Loughborough University. Available at: https://repository.lboro.ac.uk/articles/thesis/Quantitative_electroluminescence_measurements_of_PV_devices/9542582 (accessed 13 May 2025).

Figueiredo, G., Pinho Almeida, M., 2018. *Alternativa de baixo custo para imagens em eletroluminescência de módulos fotovoltaicos.* In: VII Congresso Brasileiro de Energia Solar, Curitiba, Brazil.

International Electrotechnical Commission (IEC), 2019. *IEC TS 60904-13:2019 Photovoltaic (PV) modules – Part 13: Measurement of the electroluminescence image for series resistance evaluation.* IEC, Geneva, Switzerland.

Kropp, T., Bothe, K., Schmidt, J., 2018. Determination of local series resistance values in crystalline silicon solar cells by means of electroluminescence imaging. *Solar Energy Materials and Solar Cells,* 174, 297–303.

Potthoff, A., Dullweber, T., Koduvelikulathu, L.J., Heisler, H., Hahn, G., 2010. Quantitative analysis of PV-modules by electroluminescence images for quality control. *Solar Energy Materials and Solar Cells,* 94(12), 2137–2141.

Villalva, M.G., Gazoli, J.R., Filho, E.R., 2009. Comprehensive approach to modelling and simulation of photovoltaic arrays. *IEEE Transactions on Power Electronics,* 24(5), 1198–1208.